doi: 10.1093/pasj/xxx000

Discovery of the Free Precession in the Magnetar SGR 1806−20 with the ASCA GIS

Kazuo MAKISHIMA[1,2], Nagomi UCHIDA[3], and Teruaki ENOTO[4,5]

[1] Department of Physics, The University of Tokyo, 7-3-1 Hongo, Bunkyo-ku, Tokyo 113-0033
[2] Kavli Institute for the Physics and Mathematics of the Universe (WPI), The University of Tokyo, 5-1-5 Kashiwa-no-ha, Kashiwa, Chiba, 277-8683
[3] Institute of Space and Astronautical Science, JAXA, 3-1-1 Yoshinodai, Chuo-ku, Sagamihara 252-5210, Japan
[4] Department of Physics, Kyoto University, Kitashirakawa Oiwake-cho, Sakyo-ku, Kyoto, Japan 606-8502
[5] Extreme Natural Phenomena RIKEN Hakubi Research Team, Cluster for Pioneering Research, RIKEN, 2-1 Hirosawa, Wako, Saitama, Japan 351-0198

*E-mail: maxima@phys.s.u-tokyo.ac.jp

Received 2023 December 4; Accepted 2024 April 18

Abstract

Four X-ray data sets of the Soft Gamma Repeater SGR 1806−20, taken with the Gas Imaging Spectrometer (GIS) onboad ASCA, were analyzed. Three of them were acquired over 1993 October 9–20, whereas the last one in 1995 October. Epoch-folding analysis of the 2.8–12 keV signals confirmed the ~ 7.6 s pulses in these data, which Kouveliotou et al. (1998) reported as one of the earliest pulse detections from this object. In the 1995 observation, 3–12 keV pulses were phase modulated with a period of $T = 16.4 \pm 0.4$ ks, and an amplitude of ~ 1 s. This makes a fourth example of the behavior observed from magnetars. Like in the previous three sources, the pulse-phase modulation of SGR 1806−20 disappeared at $\lesssim 2.5$ keV, where the soft X-ray component dominates. In the 1993 data sets, this periodic modulation was reconfirmed, and successfully phase-connected coherently across the 11 d interval. As a result, the modulation period was refined to $T = 16.435 \pm 0.024$ ks. The implied high stability of the phenomenon strengthens its interpretation in terms of free precession of the neutron star, which is deformed to an asphericity of $\sim 10^{-4}$, presumably by the stress of toroidal magnetic fields reaching $\sim 10^{16}$ G. Toroidal fields of this level can be common among magnetars.

Key words: Stars:individual:SGR 1806−201— Stars:magnetars — Stars:magnetic field — Stars:neutron

1 INTRODUCTION

Consider an axisymmetric rigid body with $I_1 = I_2 \neq I_3$, where I_j is the moment of inertia around the principal axes $\hat{x}_j$ ($j = 1, 2, 3$), with $\hat{x}_3$ the body's symmetry axis. When the body is free from external torque, its angular momentum $\vec{L}$ is conserved, and its dynamics around the center of gravity is split into two modes (Landau and Lifshitz 1996) that degenerate when the body is spherical. One is *free precession*, wherein $\hat{x}_3$ rotates (as seen from the inertial frame) around $\vec{L}$ with a constant precession period $P_{\rm pr} = 2\pi I_1/L$, and a constant *wobbling angle* α relative to $\vec{L}$. (This should not be confused with *forced precession* that is often observed in a spinning top.) The other is rotation around $\hat{x_3}$ with a rotation period $P_{\rm rot} = 2\pi I_3/L = P_{\rm pr}/(1+\epsilon)$, where $\epsilon \equiv (I_1 - I_3)/I_3$ is *asphericity*. When $\alpha \neq 0$ and the body's emission is symmetric around $\hat{x}_3$, we can detect $P_{\rm pr}$ as the pulsation, whereas $P_{\rm rot}$ is undetectable (see a discussion in subsection 4.3.1). If $\alpha \neq 0$ and the emission violates the symmetry around $\hat{x}_3$, the phase of the pulsation at $P_{\rm pr}$ becomes

modulated at the beat period between $P_{\rm pr}$ and $P_{\rm rot}$, given as

$$T = \frac{P_{\rm pr}}{\epsilon \cos\alpha} = \frac{1}{\cos\alpha}\left(P_{\rm rot}^{-1} - {P_{\rm pr}}^{-1}\right)^{-1} \quad (1)$$

(Butikov 2006). This *pulse-phase modulation* (PPM) provides evidence for the free precession in an asymmetrically radiating celestial object that is axially deformed ($\epsilon \neq 0$) and has $\alpha \neq 0$.

Although astrophysical examples of free precession remained relatively limited, we have detected its evidence from three magnetars; 4U 0142+61 (Makishima et al. 2014; 2019), 1E 1547.0−5408 (Makishima et al. 2016; 2021a), and SGR 1900+14 (Makishima et al. 2021b). In these objects, the hard X-ray pulses with a period $P = P_{\rm pr}$ were found to exhibit the PPM effect, with a long period of $T \sim 10^4 P$ which can be identified with T in equation (1). Further assuming $\cos\alpha \sim 1$, we find that these neutron stars (NSs) are deformed to $\epsilon \sim P/T \sim 10^{-4}$, and performs free precession.

Since the centrifugal effect is much smaller (estimated to be $\epsilon \sim 10^{-7}$) in these slowly rotating NSs, the deformation must be due to magnetic stress. Then, the inferred magnetic field becomes $B \sim 10^{16}$ G, when combined with a theoretical prediction (Ioka & Sasaki 2004) as

$$\epsilon \sim 10^{-4} (B/10^{16}\ {\rm G})^2. \quad (2)$$

Because this B is much higher than the dipole magnetic fields of these objects, $B_{\rm d} = (1-7)\times 10^{14}$ G, the magnetic fields that cause the deformation are considered to be confined inside these NSs, in the form of toroidal magnetic fields, $B_{\rm t}$.

To reinforce this scenario, we study SGR 1806−20, with the primary aim to search for the PPM effect. If this phenomenon is common to magnetars, it should also be detected from SGR 1806−20, the prototypical object which has connected the two apparently unrelated astrophysical concepts, Soft Gamma Repeaters and magnetars (e.g., Mereghetti 2008).

In all the preceding three objects (e.g., Makishima et al. 2016), the PPM was observed in their spectral hard X-ray component (HXC), but absent in their soft X-ray component (SXC). A likely interpretation is that the SXC is emitted symmetrically around $\hat{x}_3$ (which we identify with the magnetic axis), whereas the HXC breaks that symmetry. Among the known magnetars, SGR 1806−20 hosts by far the brightest HXC that extends down to ~ 3 keV (Enoto et al. 2010). Therefore, the PPM in SGR 1806−20, if any, should be detected down to ~ 3 keV, and would disappear at lower energies. To confirm this conjecture makes our second objective.

Since the first X-ray "identification" in 1993 (subsection 2.2), SGR 1806−20 was observed repeatedly by various X-ray missions. Considering the second objective, we may utilize not only hard X-ray data, but also those below 10 keV. We hence select archival 0.7–12 keV data from ASCA acquired in 1993 and 1995, for the following reasons. (1) These ASCA data provide one of the earliest information on the *persistent emission* from SGR 1806−20, and can be regarded as a start point of the investigation of this subject in SGR 1806−20. (2) As detailed later (subsection 2.1), the Gas Imaging Spectrometer (GIS) onboard ASCA is ideal to our study. (3) Because the PPM period T is expected to appear at several tens of kiloseconds, we need a total data span of $\gtrsim 50$ ks. This makes ASCA better suited than, e.g., RXTE or XMM-Newton. (4) As well known, SGR 1806−20 produced a giant flare (hereafter GF) on 2004 December 27 (e.g., Palmer et al. 2005), and since then, it showed enhanced timing noise (e.g., Younes et al. 2015), for 10 yrs or more. This could hamper our timing studies, but the ASCA data, acquired way before the GF, is expected to be cleaner in its timing behavior.

So far, we have attributed the PPM in the HXC to the free precession of a deformed NS. If this view is correct, the phase modulation, due to celestial mechanics, must have high stability. In our previous studies, consistent values of T were in fact measured in separate observations (each for 1–2 days typically) of the same source, but they were so widely apart that we were unable to coherently phase connect the PPM across them. Now, the ASCA data in 1993 were acquired in 3 separate pointings which span a total interval of 11 days. Therefore, if the PPM is detected, we can for the first time attempt to coherently phase connect the periodic modulation, across a time span which is an order of magnitude longer than was available before. This is the third objective of the present study.

2 OBSERVATIONS

2.1 The Gas Imaging Spectrometer (GIS)

The Gas Imaging Spectrometer (GIS; Ohashi et al. 1996; Makishima et al. 1996) onboard ASCA consists of a pair of identical imaging gas scintillation proportional counters, named GIS2 and GIS3. They are placed at the focal planes of the X-ray Telescope (XRT; Serlemitsos et al. 1995), and cover a wide field of view ($0^\circ.75$ diameter) with a moderate angular resolution ($\approx 4'$). The GIS also realizes a high sensitivity and a low background, over a broad energy band of 0.7–12 keV which covers both the HXC and SXC of SGR 1806−20. The modest energy resolution (8% FHHM at 7 keV) of the GIS is sufficient for the present purpose. Being gas detectors, the GIS also has a high time resolution ($\Delta t = 61$ or 488 μs) which is sufficient in the present work, together with a low dead time which allows detections of burst-like phenomena.

2.2 A brief history

We briefly review the dramatic progress of the knowledge on SGR 1806−20 that took place in the mid 1990s. As described in Murakami et al. (1994), the fourth Japanese X-ray satellite ASCA (Tanaka et al. 1994) had been in orbit for 7 months when a burst activity of SGR 1806−20 was detected, after nearly a

Table 1. X-ray data sets from the ASCA GIS utilized in the present work.

ID	Start date	MJD *	Data span†	Net exposure	Total photons‡	Flux§
G93pA	1993 October 9	49269.69	27.0 ks	15.4 ks	1990	$1.41^{+0.16}_{-0.15}$
G93pB	1993 October 10	49270.88	59.3 ks	31.7 ks	7529	$1.29^{+0.09}_{-0.08}$
G93p	(G93pA+G93pB)	—	162.1 ks	47.1 ks	9519	—
G93f	1993 October 20	49280.22	90.9 ks	39.7 ks	9613	$1.26^{+0.08}_{-0.07}$
G93T	(G93p+G93f)	—	1000.8 ks	86.8 ks	19132	—
G95	1995 October 16	50006.07	112.4 ks	58.9 ks	13556	$0.97^{+0.06}_{-0.05}$

* The Modified Julian Date of the first photon in the data.
† Gross elapsed time of the observation, from the start to the end.
‡ The total number of 0.7–12 keV events detected with GIS2+GIS3, including background.
§ Absorption-removed 2–10 keV fluxes in 10^{-11} erg s^{-1} cm^{-2}, summed over the SXC and the HXC. Errors are 90% confidence limits.

decade, by the CGRO/BATSE on 1993 September 29. At that time, the object was only coarsely ($\sim 1^\circ \times 4'$) localized by the interplanetary burst-timing triangulation.

On 1993 October 9 and 10, four short pilot pointings with ASCA were conducted, to cover the elongated error region with the wide field of view of the GIS. During one of them, onto "position-A" in Murakami et al. (1994), a short burst took place, as detected also by the CGRO/BATSE (Kouveliotou et al. 1994). Fortunately, this burst occurred at a periphery of the GIS field of view; ~ 170 signal photons were detected by GIS2+GIS3, of which about 10 were telemetered to ground with their full information (energy, position, and time). Using these 10 photons, the source was localized to an accuracy of several arcmin. An associated persistent source was also detected.

In the second of the four pilot pointings, which was onto "position-B" of (Murakami et al. 1994), the source happened to be closer to the ASCA's optical axis. Although no bursts took place, the persistent emission was detected again by the GIS, and also by the co-aligned narrower-field CCD instrument, the Solid-State Imaging Spectrometer, or SIS (Burke et al. 1991). The source location was refined by the finer position resolution of the SIS, and was named AX1805.7−2025. This has provided the "X-ray identification" of SGR 1806−20.

About 10 days later, on 1993 October 20, a follow-up ASCA pointing was made to reconfirm AX1805.7−2025. The source was observed again with ASCA in 1995 October. These follow-up observations lasted longer than the pilot pointings.

Kouveliotou et al. (1998), hereafter KEA98, combined five RXTE observations of SGR 1806−20 made in 1996 November. They discovered the source pulsation at a period of $P = 7.47655$ s, and verified that the object is a magnetized NS. They also returned to the 1993 and 1995 ASCA data, and confirmed the pulsation at 7.46851 ± 0.00025 s and 7.4738 ± 0.001 s, respectively. Based on the implied rapid spin down rate $\dot{P} = 0.8 \times 10^{-10}$ s s^{-1} from 1993 to 1996, and assuming the energy loss via magnetic dipole radiation, they concluded that the NS has a strong dipole field of $B_{\rm d} = 8 \times 10^{14}$ G. This made SGR 1806−20 the first magnetar in its genuine sense. Since then, SGR 1806−20 was observed frequently, e.g., with RXTE and XMM-Newton (e.g., Younes et al. 2015), across the 2004 December GF.

2.3 ASCA GIS data

We utilize the ASCA GIS data, acquired in 1993 and 1995, as described above and detailed in table 1. There, G93pA and G93pB denote two of the four pilot-survey pointings, at positions A and B of Murakami et al. (1994), respectively. The short burst was detected by the GIS in G93pA, whereas the source was localized by the SIS in G93pB. We also utilize the two follow-up observations, made in 1993 and 1995, as descried above; they are denoted by G93f and G95, respectively. We do not use the SIS data from any of these observations, because of the insufficient time resolution (either 2 s or 8 s).

The remaining two pointings in 1993, at "position-C" and "position-D" (Murakami et al. 1994), are not utilized, because the source was outside the GIS field of view. SGR 1806−20 was within the GIS field of view also on 1996 April 2, but its location was far from the optics axis, and the data had a short time span of ≈ 20 ks. Therefore, this data set is not used, either.

For each observation to be used, we retrieved screened 0.7–12 keV GIS events from the JAXA/DARTS Website. On-source events were extracted from a circular region of radius $0^\circ.1$ around the source, and those from GIS2 and GIS3 were coadded. The obtained backgrond-inclusive photon number is givenin table 1. The count rate is twice lower in G93pA than in the others, because the source was then farther from the XRT optical axis, where the vignetting effect is severer.

Because G93pA is short with fewer signal photons, and is separated only by ~ 1 d from G93pB, we merge together G93pA and G93pB into a single data set denoted as G93p, and mainly analyze it. This G93p has a similar number of photons to G93f, whereas its total time span, $S = 162.1$ ks, is nearly twice as long as that of G93f (S=90.9 ks). After G93p and G93f are analyzed individually, they are further merged together into a longer data set named G93T, which is utilized in more detailed

timing studies. The total time span of G93T reaches $S = 1000.8$ ks, although its net exposure is only 8.7% of this; the remaining 91.3% is data gaps, of which the longest one, from the end of G93pB to the start of G93f, is 760.6 ks (8.80 d) long.

3 DATA ANALYSIS AND RESULTS

The GIS data are analyzed without subtracting the background, which amounts to $\sim 50\%$ of the total on-source counts. Only when estimating approximate source fluxes listed in table 1, we subtract a standard background. The arrival times of these X-ray events are converted to those to be measured at the Solar-system barycenter. The data are not corrected for aspect efficiencies (collimator transmission and vignetting). Since the object was burst active in 1993, we produced a 10-s binned light curve from each data set using a broad energy range, and searched those bins where the counts exceed 2.5 sigmas above the average. In G93pA, we reconfirmed and removed the 10 burst photons (bunched in a single bin) describe in Murakami et al. (1994), whereas no bursts were detected in the other data sets.

3.1 Periodograms

In the timing studies below, we search the photon time-series data sets for periodicities, using the standard epoch-folding analysis, combined with the Z^2_m statistics (Makishima et al. 2023). The harmonic number for Z^2_m is chosen as $m = 2$ or 4, depending on the condition. The analysis incorporates the spin-down rate measured around 1993-1996, $\dot{P} = 0.8 \times 10^{-10}$ s s^{-1} (KEA98). Its effect is negligible for individual data sets (G93a, G93b, and G95), because P would change by only $\lesssim 6$ μs across each observation. However, when dealing with G93T, its effect is significant.

From G93p, G93f, and G95, we produced respective periodograms (hereater PGs) around the reported pulse periods. A harmonic number $m = 2$ was chosen for Z^2_m, because raw pulse profiles of magnetars are generally double-peaked. The energy range was set to 2.8.0–12 keV to approximately remove the SXC contribution, because differences between the soft and hard pulse profiles sometimes degrade the pulse significance. The results are shown in figure 1a superposed together. The PGs form G93p and G93f both exhibit a peak at $P \approx 7.4684$ s, and that of G95 at $P \approx 7.4738$ s. These periods are summarize in table 2, together with their 68%-confidence errors as determined in Appendix A (in particular, subsection A2 therein). Since these results agree with those which KEA98 derived from the same ASCA data, we reconfirm the pulse detections and P measurements by KEA98.

The same analysis applied to the merged data G93T, employing a finer period step of 2 μs, yielded a PG shown in figure 1b. Its behavior near the peak is expanded in figure 1c.

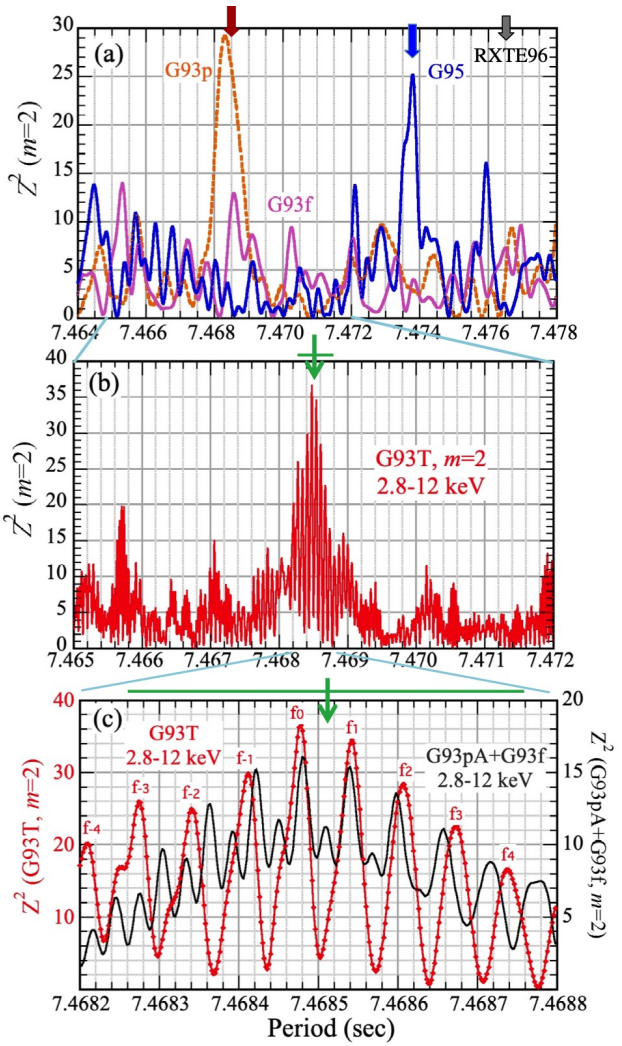

Fig. 1. Periodograms (PGs) in 2.8–12 keV with $m = 2$, showing the values of Z^2_2 as a function of the assumed period P. (a) PGs from G93p (dashed orange), G93f (magenta), and G59 (blue) are shown superposed together. Measurements by KEA98 are indicated by downward arrows. (b) A PG from G93T. The result by KEA98 is indicated by a green arrow. (c) Details of panel (b) around the peak, where the fringe numbers are given in red. The result from G93pA+G93f is superposed in black (right ordinate).

We observe a very clear fine structure, comprising a series of peaks separated by $\delta P \approx 66$ μs. Since this δP and the total data span $S = 1000$ ks of G93T approximately satisfy the relation $S \times \delta P \approx P^2$, or $S/P - S/(P + \delta P) \approx 1$, the fine structure is undoubtedly "fringes" produced by interference between the periodicities in G93p and G93f, across the ≈ 8.8 d data gap between them. For convenience, we number the fringes from -4 to +4 as in figure 1c, and denote the n-th fringe by f_n. Table 3 summarizes the parameters of these fringes.

In figure 1c, the highest fringe f_0, at $P = 7.46848$ s, has $Z^2_2 = 36.58$. Since Z^2_m obeys a chi-square distribution of $2m$ degrees of freedom, the probability for a Z^2_2 value exceeding 36.58 to appear by chance is 2.2×10^{-7} in a single trial. On the other hand, against $S = 10^6$ s, the minimum and maxim Fourier wave

Table 2. Results of the periodogram and demodulation analyses of the ASCA GIS data.*

Data	Energy †	m	Condition‡	P_0 (s)§	Z^2_m	T (ks)	$A^{\parallel}$	$\psi^{\#}$
G93p	2.8–12	2	Raw	7.46831(10)	29.2	—	—	—
	3–12	4	Demod.	7.46836(7)	46.1	$16.7^{+1.5}_{-1.1}$	0.6	270°
G93f	2.8–12	2	Raw	7.46856(11)	12.9	—	—	—
	3–12	4	Demod.	7.46856(7)	33.9	$16.5^{+0.5}_{-0.4}$	1.0	255°
G93T	2.8–12	2	Raw	7.46851(10)**	36.6	—	—	
	2.55–12	4	Demod.	7.468484(3)	63.9	16.435 ± 0.024	1.0	25°
G95	2.8–12	2	Raw	7.47380(6)	25.2	—	—	—
	3–12	4	Demod.	7.47385(4)	54.4	16.4 ± 0.4	0.9	235°

* All assuming a period change rate of 0.8×10^{-10} s s^{-1}. Errors refer to 68% confidence limits.
† The utilized energy range in keV.
‡ "Raw" and "Demod" mean without and with the demodulation, respectively.
§ The barycentric pulse period at the start of each observation, specified by the DeMD peak.
$\parallel$ The modulation amplitude A is in units of s, with a typical error by ± 0.2 s.
\# ψ has a typical error by $\pm 20°$. It should take any value in the $0 - 360°$ range.
** The error range covers four fringes from f_{-1} to f_2.

numbers covered by figure 1b are $10^6/7.472 = 133,832.9$ and $10^6/7.465 = 133,958.5$, respectively, Their difference, 125.5, represents the number of independent Fourier waves, and hence approximates the effective number of period trials. Then, the chance probability of the peak in figure 1b is estimated as $\mathcal{P}_{\rm ch} = 2.2 \times 10^{-7} \times 125.5 = 2.8 \times 10^{-5}$. This is tighter than the value of 3.6×10^{-4}, which KEA98 derived using presumably (not clearly stated in their paper) the same 1993 data sets as ours. The difference is probably because of our selection of the energy band. In fact, if we instead use 1–10 keV for instance, $Z^2_2 = 30.2$ and $\mathcal{P}_{\rm ch} = 5.6 \times 10^{-4}$ are derived.

Then, in figure 1c, which fringes other than the highest f_0 should be considered as period candidates? An obvious selection criterion is the statistical significance, as implied by the Z^2_2 values given in table 3. In Appendix A3, we evaluated the posterior probability Q_n ($n = -4$ to +4) for f_n to represent the true pulse period, all relative to $Q_0 \equiv 1$, and quote the results in table 3. Because the period could still change to some extent by the demodulation process to be conducted later, at this stage we crudely exclude only those with $Q_n < 0.01$, and conservatively retain four fringes from f_{-1} to f_2.

As another criterion, the black curve in figure 1c represents a PG from G93pA +G93f (equivalently, G93T minus G93pB), computed in the same way. All the periods here refer to the epoch of the 1st photon in the G93pA data. Although the values of Z^2_2 (right ordinate) are relatively low, we still observe the fringe pattern, of which the pitch, ≈ 60 μs, is shorter by $\sim 10\%$ than in G93T. This is because the effective data span of G93T is ≈ 10 d as mainly determined by G93pB and G93f, whereas that of G93pA+G93f is by ~ 1 d longer. Thus, a "vernier" effect is created, and δP in table 3 gives the period difference between the corresponding red and black peaks. Requiring $|\delta P| \lesssim 16$ s ($\lesssim 1/4$ of the fringe pitch), we are left with the same four fringes from f_{-1} to f_2.

Table 3. Fringe parameters in the 2.8–12 keV PG from G93T.*

Fringe num.	$P^{\dagger}_n$ (s)	Z^2_2	$Q^{\ddagger}_n$	$\delta P^{\$}$
f_{-4}	7.468 209 (9)	20.17	2.7×10^{-4}	−36
f_{-3}	7.468 275 (8)	25.96	0.0049	−30
f_{-2}	7.468 341 (8)	24.92	0.0029	−23
f_{-1}	7.468 412 (7)	29.81	0.034	−10
f_0	7.468 479 (7)	36.58	(1)	−3
f_1	7.468 542 (7)	34.54	0.36	+3
f_2	7.468 607 (9)	28.37	0.017	+9
f_3	7.468 673(11)	22.62	9.3×10^{-4}	+17
f_4	7.468 737(13)	16.55	4.5×10^{-5}	+21

* Referring to the red PG in figure 1c.
† Defined at the start of the G93pA data stream.
‡ Posterior robabilities, relative to f_0, for f_n to be the true pulse period, calculated with equation (9) in Appendix A3.
§ Period difference (in μs) of the red fringe peak, relative to the corresponding peak in the black PG.

Since the above two criteria give consistent selections, we tentatively regard f_{-1}, f_0, f_1, and f_2 as the pulse-period candidates as of 1993 October 9. In table 2, the G93T period and its uncertainty is hence defined so as to cover them. The result is consistent with those by KEA98 (green arrows in figure 1c).

3.2 Demodulation analysis

3.2.1 Formalism

Now that the pulsation has been reconfirmed in all data sets, we proceed to the *demodulation analysis*, searching the data for the PPM effects (Makishima et al. 2014; 2016; 2019). For this purpose, the arrival time of each photon (including background)

is changed from t to $t - \delta t$ using

$$\delta t = A \sin(2\pi t/T - \psi) \ , \tag{3}$$

where T, A, and ψ denote the period, amplitude, and initial phase of the assumed PPM, respectively. Then, T is varied from 7 ks to 100 ks, with a step of 0.1 ks to 0.5 ks. At each T, we maximize the pulse significance, by scanning P over a ± 0.2 ms interval (with 20 μs step) centered on the peak value in figure 1, ψ over 0° to 360° with a step of 5°, and A from 0 to 1.5 s with 0.1 s step. This range of A is chosen because A is typically $\sim P/10$, and $\sim P/4$ at most (Makishima et al. 2016). The pulse significance is evaluated with Z^2_4, where $m = 4$ is selected because the demodulated profiles of magnetar pulses usually exhibit three to four peaks (Makishima et al. 2021a). The PPM is to be found only in the HXC signals, and contamination of the SXC hampers its detection more severely than the pulse detection. We hence change the energy interval from 2.8–12 keV to 3–12 keV, to more securely eliminate the SXC contribution which could be significant up to ~ 3 keV.

3.2.2 Results from individual data sets

By applying the demodulation analysis to the 3–12 keV data from G93p, we obtained figure 2a; such a graph is called a *demodulation diagram* (DeMD), which presents, against T, the maximum Z^2_4 found at each T when A, ψ, and P are optimized. A dominant peak has appeared at $T = 16 - 17$ ks, and a sharp secondary one at $T \approx 10.5$ ks. Table 2 summarizes the parameters of the former peak; the errors (68% confidence) associated with each quantity are determined as the points where Z^2_4 falls by 4.72 from the peak value, as explained in Appendix A2 and Makishima et al. (2021a).

The 16–17 ks peak is reconfirmed in the 3–12 keV DeMD from G93f, shown in figure 2b, where T is refined to ≈ 16.5 ks (table 2). A similarly strong peak, observed at $T \approx 8.2$ ks, could be a second harmonic (half in the period and twice in the frequency). As shown in green in figure 2a and figure 2b, the pulse period depends to some extent on T. Hereafter, the value of P specified by the DeMD peak is denoted as P_0, and regarded as the best-estimated pulse period for each data set (except in G93T where the fringe ambiguity still remains).

The PPM, suggested by the two 1993 data sets, becomes compelling in figure 2c, the DeMD from G95. The peak indeed sticks out at $T \approx 16.4$ ks, and reaches $Z^2_4 = 54.4$; this is comparable to the highest DeMD peaks that were observed in the previous three magnetars (Makishima et al. 2021b). Thus, the modulation period of $T \approx 16.4$ ks $\equiv T_{16.4}$ is consistently preferred by the three data sets. They also agree on $A = 0.6 - 1.0$ s, whereas their differences in ψ do not matter, because ψ is determined solely by the start timing of the observation.

Taking the G95 DeMD as a typical case, the significance of the PPM was evaluated through a *control* study described in

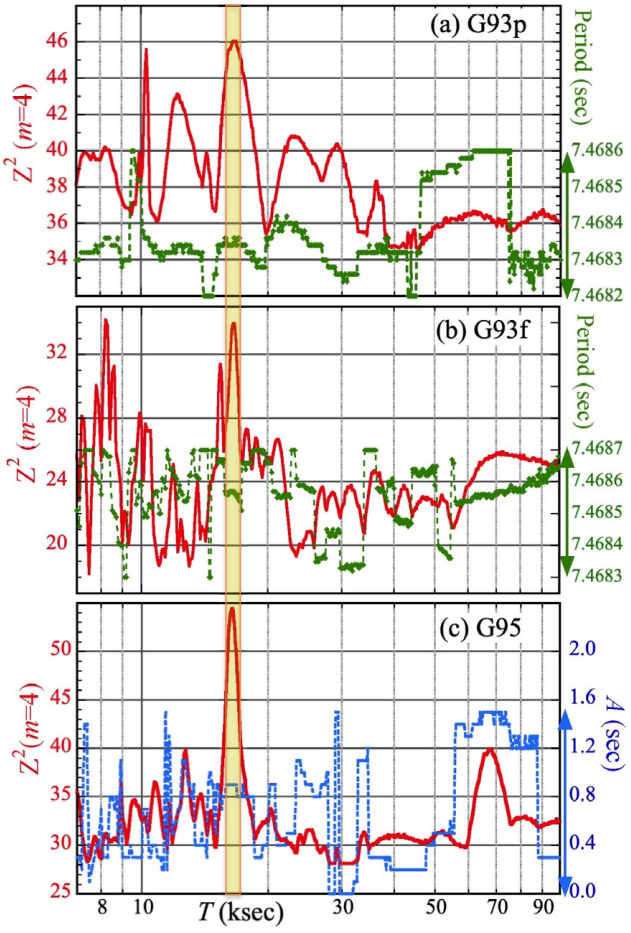

Fig. 2. DeMDs of SGR 1806−20 in 3–12 keV (in red), from (a) G93p, (b) G93f, and (c) G95, where the highest Z^2_4 value (left ordinate) is shown in red as a function of the assumed modulation period T. In (a) and (b), the best pulse period (right ordinate) is given in green, whereas in (c), the best modulation amplitude A in blue A vertical yellow stripe indicates a preferred common range of T.

Makishima et al. (2021b). That is, we derive a distribution of Z^2_4 from the same G95 data, at T shorter than $T_{16.4}$ but much longer than P, and compare the derived distribution of Z^2_4 with the value at $T_{16.4}$. As given in Appendix B, the probability for the $T_{16.4}$ peak to appear by chance, anywhere in the 7–100 ks range, is estimated as $< 1\%$. This value will further decrease when combining the G93p and G93f results. Although $T_{16.4}$ is close to three times the ASCA's orbital period, this artifact would appear at a discrepant period, 16.81 ± 0.05 ks, as judging from the data-gap recurrence in the data. We hence conclude, at 99% confidence, that SGR 1806−20 exhibits a PPM at $T \approx 16.4$ ks. Our 1st objective has been fulfilled, and SGR 1806−20 becomes the fourth magnetar exhibiting this behavior.

3.2.3 Demodulated PGs

Figure 3 provides 3–12 keV Z^2_4 PGs from the individual GIS data sets, each computed under three different conditions. Black shows a raw PG, which differs from those in figure 1a only in

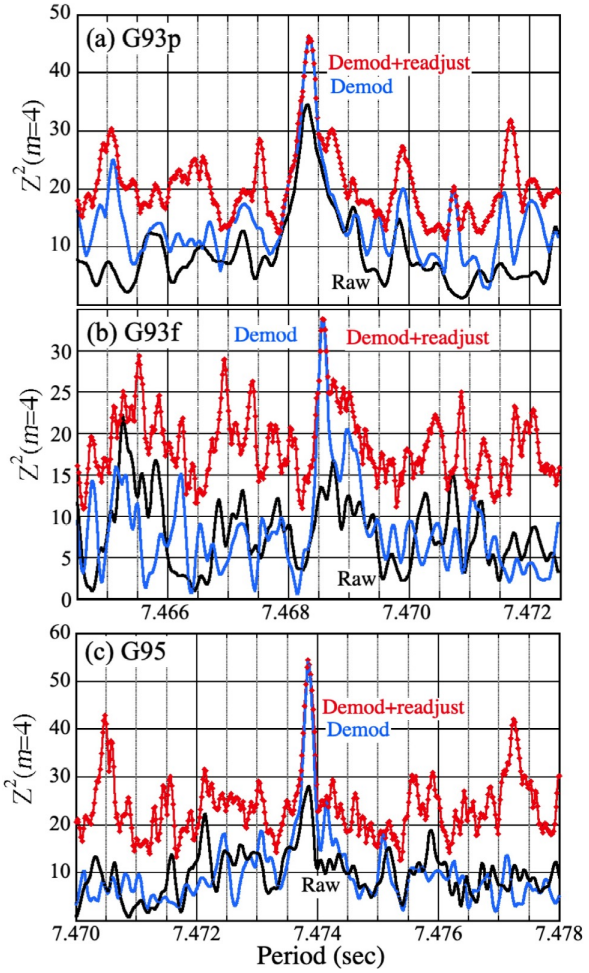

Fig. 3. PGs in 3–12 keV, derived wth $m = 4$ from the three data sets. Black PGs are simple epoch-folding results, whereas blue ones are those when the arrival times of all photons are corrected by equation (3), using a parameter triplet (T, A, ϕ) given in table 2. The red PGs are derived by readjusting the parameter triplet at each P.

the energy range and the harmonic number. The blue PG is produced through the PPM correction, where we employ, at all P, the triplet (T, A, ψ) that is optimized at $P = P_0$ (table 2). Finally, the red PGs are those in which the triplet is readjusted at each P; we let A and ψ vary in the same manner as in figure 2, whereas T over its common uncertain range, 16.0–17.0 ks (table 2) with a step of 0.1 ks. These results afford the following inferences.

1. The blue and red PGs agree well at $P \sim P_0$, where the triplet (T, A, ψ) converges to that given in table 2.
2. Except near P_0, the red PG is higher than the black and blue ones by $\delta Z_4^2 \sim 10$, due to an enlarged parameter space.
3. The demodulation enhances the pulse significance by $\delta Z_4^2 \approx$ 12, 18, and 27, in G93p, G93f, and G95, respectively. Except in G93p, these exceed the statistical increment in 2 above.
4. The red PGs (patricularly in c) exhibit a pair of sub peaks, spaced symmetrically from P_0 by $\delta P = \pm 3.4$ ms. Since $T_{16.4}\delta P \approx P_0^2$ holds, the sub peaks arise when the interval $T_{16.4}$ contains $N \pm 1$ pulse cycles, with $N \equiv T_{16.4}/P_0$. This provides additional evidence for the presence of double periodicity in the system, at P and T. The shorter sub peak can in fact be identified with $P_{\rm rot}$.
5. The demodulated PG from G93f gives $P_0 = 7.46856(7)$ s (table 2), which translates to $P_0 = 7.46849(8)$ s at the start of G93pA. This error range accommodates the fringes f_0 and $\mathrm{f}_{\pm1}$, even though the P_0 value from G93p (table 2) favors somewhat shorter fringes, e.g., f_{-3} through f_0. We retain our conservative selection made in subsection 3.1, to regard f_{-1} through f_2 as the pulse-period candidates.

3.2.4 Behavior of the softest signals

Now that our 1st objective was fulfilled, we move to the second aim, i.e., examinations whether the PPM is associated with the HXC. This is already accomplished partially, because the PPM was detected from the three data sets in the 3–12 keV interval. We however need to confirm its absence at lower energies.

As a simple examination, the lower bound energy $E_{\rm L}$ for the DeMD calculation was gradually decreased from 3.0 keV, with the upper boundary fixed at 12 keV. Then, in the G93p data, the DeMD peak at $T_{16.4}$ became higher until $E_{\rm L}$ hits ≈ 2.55 keV, beyond which the peak started diminishing. In G93f and G95, this threshold was at ≈ 2.7 keV. The inclusion of photons below these thresholds suppresses the PPM; the 3-12 keV energy range which we have selected is considered appropriate.

As a second attempt, we sort photons onto a pulse-phase vs. modulation-phase plane, and color-code the number of photons. Then, the 3–12 keV data from G95 yielded figure 4 (a1). The pulse ridges, running vertically, wiggle through the modulation phase, visualizing the PPM effect. The polar plot in figure 4 (b1) shows, as a function of A and ψ, the value of Z_4^2 achieved in the demodulation that employs $P \approx P_0$ and $T \approx T_{16.4}$. The highest Z_4^2 is found at $(A, \phi) = (0.9\ \mathrm{s}, 235^\circ)$, which is significantly displaced from the coordinate origin. In contrast, the 0.7–3 keV photons yield panels (a2) and (b2) of figurer 4. The pulse ridges are again clearly present, but they run straight. The highest Z_4^2 is hence obtained at $A \sim 0$ as in figure 4 (b2). (The higher peak at $A \approx 1.9$ s should be ignored, because we employ a limit of $A \leq 1.5$ s.) In a word, the PPM at $T_{16.4}$ is present in 3–12 keV of the G95 data, but undetectable in 0.7–3 keV.

For a further confirmation, we calculated G95 DeMDs, in seven partially-overlapping energy intervals with about the same photon numbers. The result is given in figure 5a, where black crosses show Z_4^2 at $P \approx P_0$ before the demodulation, whereas red diamonds give the increment ΔZ_4^2 attained by the demodulation. In obtaining the latter, we varied P over $P_0 \pm 60\ \mu$s, T between 16.0 and 17.0 ks, A bewteen 0 to 1.5 s, and ψ between 0° to 360°. Even though the pulse significance increases toward higher energies already before demodulation, ΔZ_4^2 rises more sharply at ~ 2 keV.

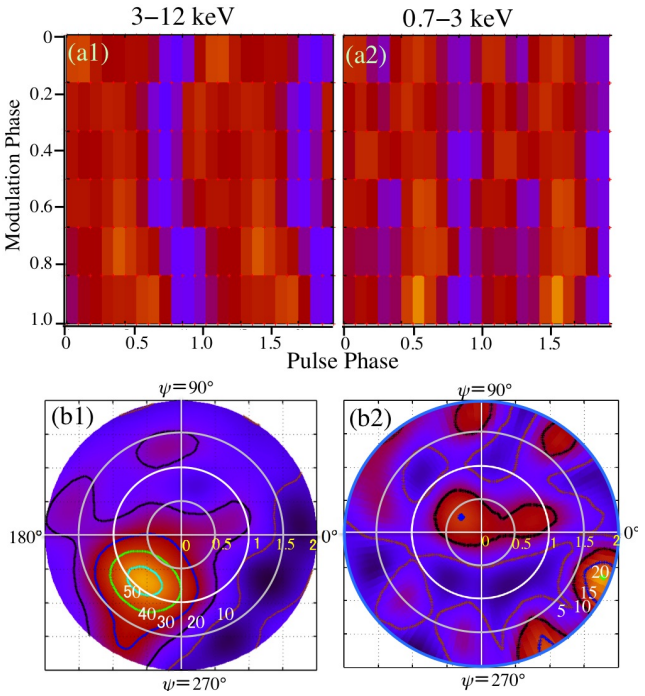

Fig. 4. Top two panels are color maps of the 3–12 keV (panel a1) and 0.7–3 keV (panel a2) photons from G95, accumulated in two dimensions, where the abscissa is the pulse phase (2 cycles) and the ordinate is the modulation phase. Bottom two panes show, on the polar coordinate (A, ψ), the maximum Z_4^2 achieved via the demodulation with equation (3). Panels (b1) and (b2) are for the 3–12 keV and 0.7–3 keV photons from G95, respectively. Contours in (b1) are from 10 to 50, whereas those in (b2) are from 5 to 20.

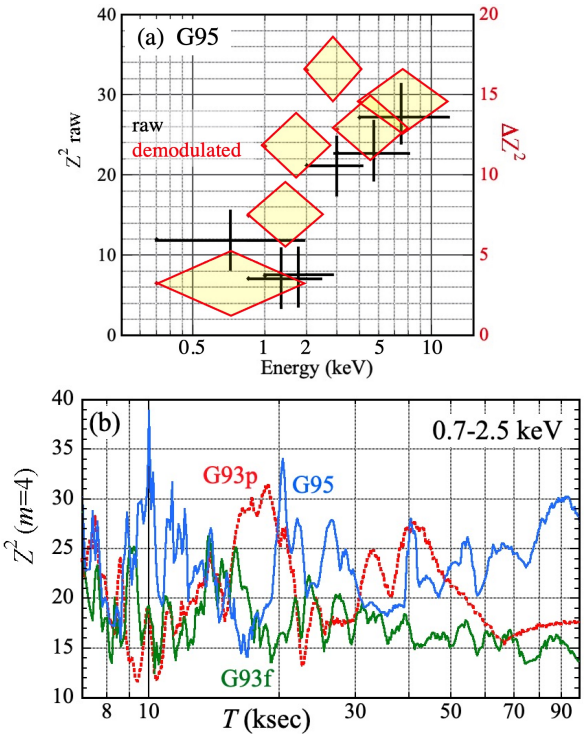

Fig. 5. (a) Pulse significance in G95 as a function of energy. Black crosses show the Z_4^2 values (left ordinate) at P_0 before demodulation, whereas red diamonds represent the increments ΔZ_4^2 (right ordinate) achieved via demodulation, of which the condition is detailed in text. (b) DeMDs in 0.7–2.5 keV, from G93p (red), G93f (green), and G95 (blue), calculated in the same way as figure 2.

To examine the behavior of the softest signals over a wider range of T, we produced 0.7–2.5 keV DeMDs from the individual data sets, and show them together in figure 5b. In the G93f and G95 results, the $T_{16.4}$ peak is no longer visible. Although the G93p DeMD exhibits a broad hump over $T = 16 - 19$ ks, it disappears when the upper energy bound is lowered from 2.5 keV to 2.1 keV. The absence of the PPM in 0.5–2.5 keV is considered intrinsic, rather than due to insufficient statistics.

Through these multiple examinations, we consistently found that the PPM in SGR 1806−20 is present in energies above ~ 3 keV, whereas it is absent or much suppressed below ~ 2.5 keV. This means an affirmative answer to our second aim.

3.3 Demodulation analysis of the joint G93T data

3.3.1 Procedure

Our remaining task is to apply the demodulation analysis to the merged G93T data, hoping to coherently phase-connect the 16.4 ks PPM across the 11-d time span which is dominated by the 8.8-d data gap. If the modulation period T is coherent, it will also exhibit an interference structure, like in figure 1c, this time with a separation of $\Delta T \approx T^2/S \approx 0.27$ ks. Thus, the search step in T is selected to be 0.005 ks. To cover the four surviving fringes from f_{-1} to f_2 (figure 1c), we scan P from 7.46838 s to 7.46862 s with a step of 2 μs (the same as in figure 1c). In contrast, A and ψ are treated in the same way as before, because they are free from the interference. Similarly, we retain $\dot{P} = 0.8 \times 10^{-10}$ s s^{-1}, which is now quite essential. Based on the examination in § 3.2.4, the energy range is changed from 3–12 keV to 2.55–12 keV to increase the signal statistics, with the photon number increasing from 10971 to 12758.

3.3.2 Results

The 2.55–12 keV DeMD thus derived from G93T is presented in figure 6 in red. As expected, we again observe clear interference peaks denoted as A through G, with an average pitch of ~ 0.3 ks. Hereafter, we call these peaks "T-fringes", to distinguish them from those in P. The structure is somewhat more complex than that in figure 1c, and the pitch varies. These properties are thought to arise because we now treat double periodicity, in P and in T. The highest T-fringe, D ($Z_4^2 = 63.86$), occurs at $T = 16.435$ ks, in a good agreement with the peak of the 3–12 keV G95 DeMD, which is superposed by a dotted black curve with a positive offset by 7. As shown in dotted horizontal lines in blue, the T-fringe D is associated with $P = 7.468484$ s (table 2), which coincides with f_0 in figure 1c.

Over $T = 16 - 17$ ks in figure 6, the envelope of the red curve, encompassing several T-fringe peaks such as C, C', D,

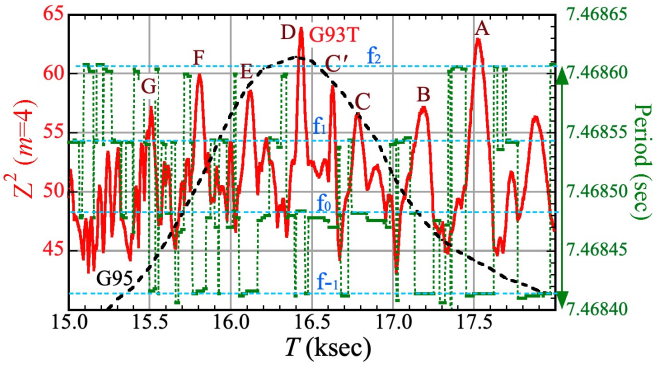

Fig. 6. A 2.55–12 keV DeMD from the combined G93T data (red), compared with the 3–12 keV DeMD from G95 (black). The latter is the same as in figure 2c, but is given a positive offset by 7 just for presentation. Green data points show P (right ordinate) associated with the G93T DeMD. Dotted horizontal lines in cyan indicate the four surviving fringes from figure 1c. Peaks denoted as A through G are discussed in text.

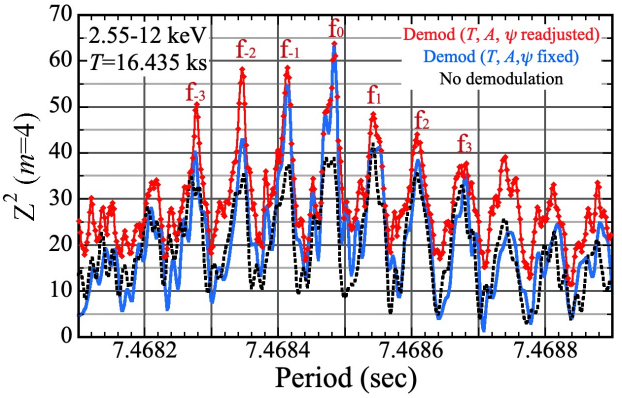

Fig. 7. PGs from the joint G93T data, calculated in 2.55–12 keV with three different ways as in figure 3. See text for details.

and E, is similar to the G95 DeMD. Furthermore, in this interval, the optimum P mainly stays on f_0, except several excursion episodes. Outside this T interval, in contrast, the G93T DeMD decreases much more slowly than that of G95, and shows several "outlier" peaks such as A, B, F, and G. Since they all belong to the period fringes other than f_0, they are thought to arise when pulse-phase mismatches across the long data gap, due to incorrect values of P, are mitigated by changing T.

Although D is highest in figure 6, the T-fringe A has nearly the same heigh; C' and F might also be considered. This urges us to evaluate relative significances of these T-fringe peaks. The procedure is similar to that for the period fringes made in section 3.1 and Appendix A3. This time, however, we can use the G95 DeMD (black in figure 6) as *prior* probability, assuming T to be the same between 1993 and 1995. Then, the Bayes' theorem tells us how our knowledge on T improves by adding the G93T DeMD. We performed this evaluation in Appendix A4, and derived the *posterior* probability for each T-fringe to represent the true value of T. As a result, the peaks other than D were all found to have a probability which is $\lesssim 3.4\%$ relative to D (with C' the next most likely). We can hence conclude, at 95% confidence, that D is the correct peak, and derive

$$T = 16.435 \pm 0.024 \text{ ks} \quad (T-\text{fringe D}) \tag{4}$$

as of the beginning of G93pA.

3.3.3 Demodulated PGs from G93T

In figure 6, the best T-fringe D specifies f_0 as the best pulse period; this combination can be expressed as (D, f_0). However, it is not yet clear whether the other combinations such as (D, $f_{\pm1}$) can be statistically ruled out. To answer this issue, figure 7 shows 2.55-12 keV PGs ($m = 4$) from G93T, calculated under three different conditions like in figure 3. The dotted black curve is the PG without demodulation, which is similar to figure 1c but differs in the energy range and m. The blue one is a demodulated PG, in which we fix T to equation (4), as well as $A = 1.0$ s and $\psi = 25°$ as specified by the T-fringe D of figure 6. When A and ψ are left to float at each P, and T is allowed to vary within ± 0.03 ks of equation (4), the red PG is obtained.

The red PG in figure 7 gives $Z_4^2 = 63.86$ for (D, f_0), whereas $Z_4^2 = 58.48$ for the next highest candidate, (D, f_{-1}). According to the consideration in Appendix A4, their height difference, $X = -\delta Z_4^2 = 5.38$, implies that the relative probability for (D, f_{-1}) to be the true solution is $\exp(-5.38/2) = 6.8\%$ of that of (D, f_0). The candidates (D, f_n) with $n \neq 0$ are hence excluded at 90% or higher confidence, and the pulse period as of the start of G93pA is determined as

$$P = 7.468\,484(3) \text{ s} \quad (\text{fringe } f_0). \tag{5}$$

If calculated in the same 2.55-12 keV interval as the G93T DeMD, the G95 DeMD (thought not shown) has the maximum of $Z_4^2 = 55.58$. Because G93T has 1.4 times more photons than G95 (table 1), and Z_4^2 is proportional to the signal photon number if the folded profile is similar, we expect the peak D to reach $Z_4^2 = 77.8$. The actually observed peak D height, $Z_4^2 = 63.86$, is 82% of the prediction. In addition, Z_4^2 is proportional to the squared pulse fraction of the relevant periodicity, where the pulse fraction is defined as $(H_+ - H_-)/(H_+ + H_-)$, using the peak height H_+ and the bottom height H_- of a folded pulse profile. Accordingly, we infer that the PPM has been phase-connected across the 11-d time span with a good phase coherence of $\sqrt{0.82} = 0.91$.

In this way, the demodulation of the merged G93T data in 2.55–12 keV enabled us to confirm the coherence of the PPM cycle across the 11-d interval, and measure its period T with an unprecedented accuracy of 0.15%. These are thanks to the particular observation patter in 1993, and to the shortest T among the four magnetars exhibiting the PPM. Thus, our 3rd objective has also been fulfilled. At the same time, the demodulation analysis successfully resolved the period ambiguity which was identified in figure 1c.

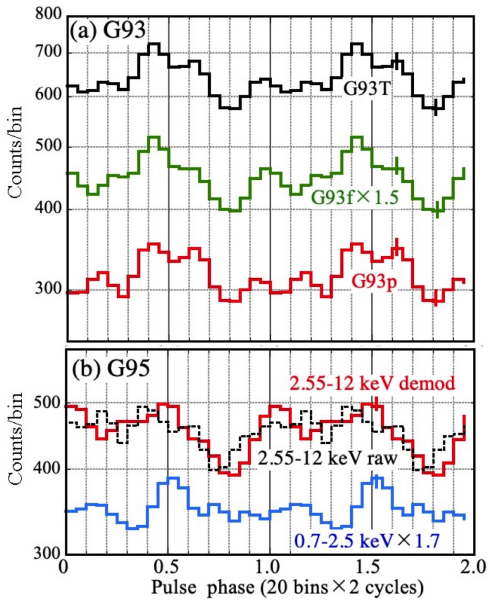

Fig. 8. Background-inclusive pulse profiles of SGR 1806−20 from the GIS data sets, shown for two pulse cycles after applying the running average (see text). (a) Results in 2.55–12 keV from G93p (red), G93f (green) multiplied by 1.5, and G93T(black). They are all folded using a common solution (see text). (b) The 2.55-12 keV profiles from G95, before (black) and after (red) the demodulation. The phase origin is manually adjusted to that of (a). A 0.7–2.5 keV profile, folded without demodulation, is presented in blue.

3.3.4 The spin-down rate

From the 1993 and 1995 period measurements (table 2) across a span of ≈ 2 yrs, the average spin-down rate is derived as 0.84×10^{-10} s s^{-1}, in agreement with KEA98. In addition, the long time span of G93T may allows us to estimate the instantaneous $\dot{P}$ in 1993 September. By changing it from 0 to 1.5×10^{-10} s s^{-1}, we studied how Z_4^2 of the demodulated 2.55-12 keV pulses from G93T varies. As a result, a loose constraint as $\dot{P} = (0.77 \pm 0.63) \times 10^{-10}$ s^{-1} (68% confidence) was obtained. From these two estimates, our assumption of $\dot{P} = 0.8 \times 10^{-10}$ s^{-1}, which has so far been employed, is confirmed to be appropriate.

3.4 Pulse profiles

In figure 8, we compile background-inclusive folded pulse profiles obtained from the GIS data. They are smoothed with a running average as described in Makishima et al. (2021a), so the error associated with each bin is 0.61 times the Poissonian value. The ordinate is logarithmic, to enable a direct comparison of the pulsed fraction among the profiles. Although the 2.55–12 keV photons are used here, the results are very similar even if using the 3–12 keV interval.

Figure 8a compares 2.55–12 keV profiles from G93p, G93f, and G93T. They are all obtained using a common solution specified by equation (5) and equation (4), together with A and ψ for G93T in table 2, and shown against a common pulse phase. The three profiles are reasonably similar, with the deep minimum at a pulse phase 0.8, and nearly the same pulse fraction. These demonstrate that the pulse phase has been successfully connected through the 11-d interval. The G93p result comprises equally-spaced four peaks, whereas two of them become dominant in the G93f result.

Figure 8b compares the 2.55–12 keV profiles from G95, before (dashed black) and after (red) the demodulation. The demodulated profile is approximately double peaked, which is closer to the G93f profile than to that in G93p. This kind of mild profile variations are often seen in magnetars (Makishima et al. 2021b). Also shown is the 0.7–2.5 keV raw profile, representing the SXC pulses, to be compared with panel (a2) of figure 4.

4 Discussion

4.1 Summary of the results

We analyzed the 0.7–12 keV X-ray data of SGR 1806−20 acquired with the ASCA GIS, on three occasions in 1993 October (G93pA, G93pB, and G93f), and once in 1995 October (G95). The aims are threefold; to search for the PPM phenomenon, to confirm its association with the spectral HXC, and to coherently connect the PPM phase across the 11-d interval spanned by the merged 1993 data (G93T=G93p+G93f).

The periodogram analysis with $m = 2$ (figure 1a), using 2.8–3 keV photons from G93p, G93f, and G95, individually yielded the pulse periods as in table 2. The combined data G93T revealed a clear interference pattern (figure 1c), and the probability for the highest fringe to appear by chance fluctuations was estimated as $\mathcal{P}_{\rm ch} = 2.8 \times 10^{-5}$ taking into account "look-elsewhere" effects. These results reconfirm the pioneering work by KEA98 who analyzed the same GIS data.

To these data sets, we next applied the demodulation analysis using the 3–12 keV energy interval and $m = 4$. Then, the G95 data gave a highly significant ($\gtrsim 99\%$; Appendix B) DeMD peak at $T \approx 16.4$ ks (figure 2c). The same effect, though weaker, was confirmed in the 3–12 keV DeMDs from G93p (figure 2a) and G93f (figure 2b). We hence conclude that SGR 1806−20 is the fourth magnetar exhibiting the PPM phenomenon, with the shortest T. The effect was confirmed down to ~ 2.5 keV, but absent in lower energies (figure 4b, figure 5). Thus, the 1st and second aims of the research have been accomplished.

Finally, we applied the demodulation analysis to the merged G93T data in 2.55–12 keV, and successfully connected the PPM phase through the entire G93T data, which is 11-d long, or about 58 modulation cycles. We thus confirmed the PPM to have high stability, and determined T with an unprecedented accuracy of 0.15%. The demodulation resolved the period ambiguity in figure 1c, and yielded equation (5) and equation (4). In short, we successfully achieved the third objective as well.

Table 4. PPM parameters of the four magnetars.

Source	Data *	Energy (keV)	P (s)	T (ks)	P/T (10^{-4})	$B_{\rm t}^{\dagger}$	$B_{\rm d}^{\ddagger}$	$B_{\rm t}/B_{\rm d}$	$\tau_{\rm c}^{\S}$ (kyr)	Ref.$^{\|}$
4U 0142+61	Suzaku (07)	15–40	8.6888	PPM not detected						[1,2]
	Suzaku (09)	15–40	8.6889	55 ± 4	1.6	1.3	1.3	100	68	[2]
	Suzaku (13)	15–40	8.6891	54 ± 3	— the same as above —					[3]
	NuSTAR (14)	10–70	8.6892	54.8 ± 5.3	— the same as above —					[3]
SGR 1900+14	Suzaku (09)	12–50	5.210	41.2 ± 1.2	1.3	1.1	7.0	16	0.90	[4]
	NuSTAR (16)	6–20	5.227	40.5 ± 0.8	— the same as above —					[4]
1E 1547.0−5408	Suzku (09)	10-30	2.072	$36.0^{+4.5}_{-2.5}$	0.58	0.76	3.2	24	0.69	[5]
	NuSTAR (16)	8–25	2.087	36.0 ± 2.3	— the same as above —					[6]
SGR 1806-20	ASCA (93)	2.55–12	7.4685	16.435(24)	4.5	2.1	20	11	0.24	This work
	ASCA (95)	3–12	7.4739	16.4 ± 0.4	— the same as above —					This work

* The utilized data, and the last two digits of the observation year in parenthesis. The results from the Suzaku XIS are not shown.
† Toroidal magnetic fields in units of 10^{16} G, calculated with equation (2) assumig $\cos\alpha \sim 1$.
‡ Surface dipole magnetic fields in 10^{14} G, calculated as $\propto (P\dot{P})^{1/2}$, taken from McGill Online Magnetar Catalog (http://www.physics.mcgill.ca/ pulsar/magnetar/main.html)
§ Characteristic age $\tau_{\rm c} \equiv P/2\dot{P}$.
‖ References: [1] Enoto et al. (2011); [2] Makishima et al. (2014) ; [3] Makishima et al. (2019); [4] Makishima et al. (2021b); [5] Makishima et al. (2016); [6] Makishima et al. (2021a);

4.2 Ubiquity of the phenomenon

Among about 30 magnetars known to date, SGR 1806−20 is the prototypical object with extreme activity, showing the highest $B_{\rm d}$ and the shortest characteristic age, $\tau_{\rm c} \equiv P/2\dot{P}$. Therefore, SGR 1806−20 was a sort of "touchstone" to assess whether the PPM is generally seen among magnetars. The present result has indeed given an affirmative answer to this anticipation.

Table 4 summarizes the basic PPM parameters of the four magnetars (including SGR 1806−20) that exhibit this phenomenon. Regarding G93T and G95 of SGR 1806−20 as two independent data, so far the 10 data sets listed in this table have been analyzed for the PPM effect. It was detected successfully from all these data, except the 2007 Suzaku observation of 4U 0142+64. Therefore, the PPM must be ubiquitous among magnetars. The sole exception may be explained if the PPM amplitude then happened to be very small, e.g., $A \lesssim 0.05P$, as actually found with NuSTAR in 2009 (Makishima et al. 2021a) thanks to its higher sensitivity than the Suzaku HXD.

When studying a new phenomenon like the present subject, we must carefully exclude instrumental artifacts. In this respect, the present result is of high value, because it means that the PPM in the four magnetars has been confirmed by four instruments; the HXD and the XIS onboard Suzaku, NuSTAR, and the ASCA GIS. They respectively utilize non-imaging Silicon PIN diodes, X-ray CCD devices, pixellated CdZnTe detectors, and imaging gas scintillation proportional counters, with the latter three coupled with X-ray focusing telescopes. The detections with these distinct types of X-ray detectors, onboard three different spacecrafts, is thought to minimize the risk of the phenomenon being of some instrumental origin.

It is intriguing to examine how the PPM phenomenon in magnetars (including SGR 1806−20) remained undetected until 2014. Presumably, past timing studies of magnetars mostly utilized SXC-dominated energies (e.g., $\lesssim 10$ keV) which are usually free from the PPM disturbance. Even when the utilized instrument (e.g., RXTE) covers HXC-dominated energy ranges, usually the period found in the softer band was used to produce folded pulse profiles in harder X-rays, without examining whether the pulse is significant therein or not. Obviously, the situation is different for SGR 1806−20 in which the HXC dominates down to ~ 3 keV, but probably the pulse detection in this particular object was possible without demodulation, as we have experienced (figure 1). The PPM perturbation might be smeared out due to the short T.

For reference, our first detection of the PPM phenomenon, from 4U 0142+61 (Makishima et al. 2014), was enabled by good fortune. The 15–40 keV Suzaku HXD data of this object, acquired in 2007, allowed the pulse detection via a standard periodogram analysis (Enoto et al. 2011). In contrast, from the HXD data acquired in 2009, the same analysis in the same energy band failed to detect the pulsation, in spite of very similar exposures and source intensities. Presumably A changed as mentioned above. This discrepancy between the two observations drove us to the PPM discovery.

4.3 Astrophysical implications

4.3.1 The free-precession interpretation

As describe in section 1, the PPM effect in magnetars has so far been interpreted as a manifestation of the free precession of an NS that is axially deformed to $\epsilon \approx P/T \sim 10^{-4}$. In table 4, the ratio $P/T = 4.5 \times 10^{-4}$, which we find for SGR 1806−20, is higher than, but still of the same order as, those of the other three magnetars. Moreover, the modulation amplitude of SGR 1806−20, $A = 0.6 - 1.0$ s (table 2) or $(0.08 - 0.13)P$,

Table 5. Classification of rotational motions of a rigid body.*

Case	Mode of rotation	Condition† (i)	(ii)	(iii)	T of eq.(1)	Pulse detection
A1	Spherically	yes	yes	yes	∞	no
A2	symmetric	yes	yes	no	∞	$P_{\rm rot}(=P_{\rm pr})$
A3	rotator	yes	no	‡	∞	$P_{\rm pr}(=P_{\rm rot})$
B1	"Sleeping"	no	yes	yes	finite	no
B2	rotator	no	yes	no	finite	$P_{\rm rot}$
C1	Free	no	no	yes	finite	$P_{\rm pr}$
C2	precession	no	no	no	finite	$P_{\rm pr}\times$PPM

* Non-axi-symmetric deformation is not considered.
† See text for the meaning of the three conditions.
‡ The pulse behavior does not depend on this condition.

agrees with those of the others. Therefore, the free-precession interpretation will apply also to this prototypical magnetar.

By the successful phase connection through the G93T data spanning 1000 ks, the PPM in SGR 1806−20 was confirmed to have good coherence for at least ~ 60 cycles. As a result, T was determined with an accuracy of 0.15%. These results mean large improvements over our past knowledge, where the reproducibility of T of each object was confirmed only to an accuracy of $\sim 10\%$ (table 3). We can now regard the PPM as a stable periodic phenomenon, rather than some transient quasi-periodicity. Since such high stability is likely to arise via celestial mechanics, the free precession scenario is greatly reinforced.

The overall phenomenon may be understood by considering the following three symmetry conditions, which describe an axisymmetric rigid rotator emitting radiation (Butikov 2006).

(i) The object is spherically symmetric; namely, $\epsilon = 0$.
(ii) The symmetry axis $\hat{x}_3$ is aligned with $\vec{L}$; namely, $\alpha = 0$.
(iii) The emission is axially symmetric around $\hat{x}_3$.

Then, the pulse detectability can be classified as in table 4, according to whether each condition holds (denoted by "yes") or is violated (denoted by "no"). Among the total seven cases, A2 and A3 apply to ordinary spherical pulsars. These two are in reality equivalent, because A3 reduces to A2 if $\hat{x}_3$ is redefined as a unit vector parallel to $\vec{L}$.

The remaining cases ($\epsilon \neq 0$) can be best explained in terms of a spinning rugby ball, which obviously violates the condition (i). When the ball is spinning precisely around $\hat{x}_3$ ($\alpha = 0$), and if its appearance is symmetric around $\hat{x}_3$, we can never tell that the ball is spinning (case B1). However, if the ball has a "logo mark" pained on its side, (iii) is violated, and we can detect the spin by the logo's recurrence. This corresponds to B2, and the observed pulse period P gives $P_{\rm rot}$, with $P_{\rm pr}$ undetectable.

If $\alpha \neq 0$ instead, the rugby ball wobbles, in such a way that its tips rotate around $\vec{L}$ with a period $P_{\rm pr}$, which satisfies $P_{\rm pr} : P_{\rm rot} \approx 5 : 3$. If the ball has no logo [(iii) satisfied], we can detect only $P_{\rm pr}$ via the tip recurrence. This is the case C1, wherein the pulse period to be observe is $P_{\rm pr}$ rather than $P_{\rm rot}$ (secion 1). This condition accounts for the magnetar SXC, which may be emitted isotropically from the magnetic poles (=around $\hat{x}_3$) . Finally, the HXC of magnetars corresponds to C2, wherein the basic periodicity is still $P_{\rm pr}$, but it is coupled with $P_{\rm rot}$ to exhibit the PPM; the amplitude A depends on α, the degree of emission asymmetry around $\hat{x}_3$, and our viewing angle to the system (Makishima et al. 2021a).

Identifying the observed P of a magnetar with $P_{\rm pr}$ may contradict to the common belief to identify P with $P_{\rm rot}$. However, $P_{\rm pr}$ and $P_{\rm rot}$ of a magnetar differ by ony $\sim 10^{-4}$, and both are directly proportional to L, with their ratio kept strictly constant (assuming ϵ and α to be constant). Hence, $P_{\rm pr}$ and $P_{\rm rot}$ increase together due to the same mechanism, namely, a decrease in L through, e.g., the magnetic dipole radiation. If a rugby ball with $\alpha \neq 0$ spins down, its wobbling inevitably gets slower, too. Thus, the general framework of estimating $B_{\rm d}$ and $\tau_{\rm c}$, from the observed P and $\dot{P}$, still remains intact.

When L of the object is conserved and its kinetic energy decreases, the wobbling angle α approaces 0 if the deformation is oblate ($\epsilon < 0$), whereas $|\alpha|$ increases if prolate ($\epsilon > 0$). At present, the observations are unable to tell whether the deformation of these magnetars is oblate or prolate. Nevertheless, we believe that the deformation is prolate, because α would then develop, with no external perturbation, to a finite level, even if it was initially very small.

4.3.2 Toroidal magnetic fields of magnetars

Taking the free-precession scenario for granted, we can think of three origins of the deformation; centrifugal force, magnetic stress of $B_{\rm d}$, and that of $B_{\rm t}$. The deformation from the first two origins will be oblate, and are too small to explain $|\epsilon| \sim 10^{-4}$. In contrast, the toroidal field hidden inside the NS will cause a prolate deformation. Furthermore, if $B_{\rm t} \sim 10^{16}$ G, the deformation will be large enough to explain the observation as in equation (2). Using this relation, we calculated $B_{\rm t}$ and give the results for the four magnetars in table 4, together with their $B_{\rm d}$ and $\tau_{\rm c}$. Thus, the four objects are all inferred to harbor ultrastrong toroidal magnetic fields, $B_{\rm t} \sim 1 \times 10^{16}$ G.

Importantly, table 4 comprises objects in all the three major subclasses of magnetars: two Soft Gamma Repeaters (SGR 1900+14 and SGR 1806−20), an Anomalous X-ray Pulsar (4U 0142+61), and one transient magnetar (1E 1547.0−5408). When combined with the discussion in subsection 4.2, this suggests that essentially all magnetars harbor $B_{\rm t} \sim 10^{16}$ G, even though the examples are still limited at present.

The four objects in table 4 are arranged in the descending order of their $\tau_{\rm c}$. We observe a trend of the $B_{\rm t}/B_{\rm d}$ ratio to increase toward older magnetars. Therefore, the toroidal fields of magnetars possibly last longer than their dipole fields (Makishima 2023). This evolution, if confirmed with a larger sample, will naturally explain the presence of such NSs as

weak-field magnetars (e.g., Rea et al. 2014). It is however not obvious whether the activity of magnetars is powered by $B_{\rm d}$ which is weaker but supposedly more easily dissipated, or $B_{\rm t}$ which is stronger but could be more difficult to utilize. In any case, we need a larger sample. In addition, a more quantitative study is necessary, because $\tau_{\rm c}$ of magnetars, which is calculated assuming a constant $B_{\rm d}$, is likely to overestimate their true age (Nakano et al. 2015).

4.3.3 The two spectral components of magnetars

Persistent X-ray spectra of magnetars are known to consist generally of the HXC and the SXC (section 1; Enoto et al. 2010), which are characterized respectively by a blackbody-like spectral shape and a hard power-law form. In 4U 0142+61, 1E 1547.0−5408, and SRG 1900+14, the PPM was found to disappear below ~ 10 keV, ~ 8 keV, and ~ 6 keV, respectively, which are close to their HXC vs SXC cross-over energies. Therefore, he PPM perturbation was suggested to affect only the HXC pulses (e.g., Makishima et al. 2016).

In the present work, we utilized the very bright HXC of SGR 1806−20, to confirm that the PPM is present down to ~ 2.55 keV, again close to the cross-over energy of the two components. The exclusive association of the PPM with the HXC has been reinforced. The presence/absence of the PPM at a given energy is likely to be determined by the relative dominance of the two components at that energy, rather than the absolute value of the energy itself.

As mentioned with respect to table 5, a likely origin of this HXC vs SXC difference is their distinct emission patterns; the SXC is probably emitted axi-symmetrically around the star's symmetry axis, whereas the HXC breaks that symmetry. Possible geometries and some inference on the HXC emission process are already described previously (e.g., Makishima et al. 2016; 19; 21a), which we do not repeat here.

4.4 Future prospects

Utilizing the earliest pulse detections from SGR 1806−20, the present results have provided literally the starting point of the study of non-spherical dynamics of this prototypical object. We may point out several future prospects.

One aspect of interest with SGR 1806−20 is whether any noticeable change took place in ϵ or α, across the 2004 GF which was presumably caused by a sudden release of internal magnetic energies (of $B_{\rm d}$ and/or $B_{\rm t}$). By analyzing rich X-ray data taken after 2004 December (e.g., with XMM-Newton, Suzaku and NuSTAR), and comparing with the present results, some information may be obtained.

The free-precession interpretation of the PPM effects predict $T \propto P$ as in equation (1), assuming ϵ and α both constant. To verify this relation of high importance, SGR 1806−20 is indeed ideal, because of its rapid spin down and the shortest T. This attempt will be carried out in future, together with the above study of the source behavior across the GF.

Putting aside SGR 1806−20, another future task is to examine the suggested time evolution of the $B_{\rm t}/B_{\rm d}$ ratio (subsubsection 4.3.2). For this purpose, we need to detect the PPM and measure T from magnetars with intermediate ages, in between SGR 1806−20 and the other three in table 4. Promising candidates include SGR 0501+4516, 1RXS J170849.0−400910, and 1E 1841−045, which have $\tau_{\rm c} = 15$ kyr, 8.9 kyr, and 4.6 kyr, respectively. In fact, some preliminary information was derived affirmatively from some of them (Makishima 2023).

5 Conclusions

We analyzed the 0.7–12 keV ASCA GIS data of SGR 1806−20, taken on three (effectively two) occasions in 1993 October, and another in 1995 October. The pulses, previously detected by KEA98 using the same data, were reconfirmed, at consistent periods of 7.4685 s in 1993 and 7.4738 s in 1995.

In all data sets, the 3–12 keV pulses were found to suffer the PPM effect, with a modulation period of $T \approx 16.4$ ks and an amplitude of $A \approx 1$ s. Thus, SGR 1806−20 becomes a fourth magnetar exhibiting this phenomenon, with the shortest T, after 4U $0142-61$, 1E 1547.0−5408, and SGR 1900+14. The PPM effect must be ubiquitous among magnetars.

The PPM in SGR 1806−20 is present in energies above ~ 2.5 keV, but absent in lower energies. As inferred from the previous three magnetars, the PPM is thus associated exclusively with their HXC, and absent in their SXC.

Using the merged 1993 data, the PPM was confirmed to persist coherently for a 11-d interval, with a refined period of 16.453 ± 0.024 ks. Therefore, the PPM is a highly stable phenomenon, and its interpretation in terms of the free precession (and the associated beat effect) is much reinforced.

Including these four examples, all magnetars may be axially deformed to $\epsilon \sim 10^{-4}$, which in turn is ascribed to toroidal magnetic fields reaching $B_{\rm t} \sim 10^{16}$ G. All magnetars are hence suggested to harbor toroidal magnetic fields of this strength. In addition, $B_{\rm t}$ of magnetars may last longer than their $B_{\rm d}$.

Acknowledgements

The present work was supported in part by the JSPS grant-in-aid (KAKENHI), number 21K03624. KM thanks Dr. Hiroki Yoneda for his helpful advices.

Appendix A: The Z_m^2 statistics

We explain how to estimate errors in the period determination in a Z_m^2 PG, and how to distinguish among multiple period candidates seen there.

A1: Z^2_m and the likelihood function

Let $Z^2_m(P)$ represents a PG calculated from an un-binned time series, like the present case, using the Z^2_m statistics. If a particular period P_1 gives a high value of $Z^2_m(P_1)$, we regard P_1 as having a high "likelihood" to represent the true period P^*. In fact, as shown by Yoneda (2020), the so-called likelihood function $\mathcal{L}(P)$ (see, e.g., Appourchaux et al. 1998 for its definition), calculated from the same time series, satisfies a relation

$$Z^2_m(P) \approx 2\log \mathcal{L}(P)\ , \tag{6}$$

as long as the number of photons is sufficiently large, the data are dominated by Poisson noise, P lies in a vicinity of P^*, and $\mathcal{L}$ around P^* distributes as a Gaussian. Note that $\mathcal{L}(P)$ is not a probability density, because we are using a limited amount of data to estimate the underlying probability density function that is unknown.

A2: Errors in the period determination

When a PG becomes highest at a period P_0, it obviously provides the most likely (maximum likelihood) candidate for P^*. However, we need to estimate the error associated with P_0Ḣence, using equation (6), we define an associated variable

$$X(P) \equiv Z^2_m(P_0) - Z^2_m(P) \approx 2\log[\mathcal{L}(P_0)/\mathcal{L}(P)] \geq 0, \tag{7}$$

which is just the *decrement* in $Z^2_m(P)$. Then, the process of maximizing $Z^2_m(P)$ turns into a process of minimizing $X(P)$.

Suppose that the $X(P)$-minimum point P_0 is close to P^*, and $X(P)$ is Gaussian distributed around P_0. Then, as explained in Yoneda (2020) and quoted by Makishima et al. (2021a), $X(P)$ obeys a chi-square distribution of n degrees of freedom, where n is not the harmonic number m, but the degree of freedom involved in the $X(P)$-minimization process.

A simple periodogram has $n = 1$, because P is the only variable. The 68% and 90% confidence error regions are specified by the condition that $X(P)$ reaches 1.0 and 2.71, respectively. When the demodulation process is incorporated, we should instead use $n = 4$ (regardless of m), because the four parameters, P, T, A, and ψ, are optimized to find minimum point with $X(P) = 0$. Then, the 68% and 90% confidence regions are determined by $X(P) = 4.72$ and $X(P) = 7.78$, respectively. In table 2 and table 3, the errors associated with P and the other parameters are determined in this way, for both the raw and demodulated PGs, employing the 68% convention.

A3: Identification of the most likely period fringe

When a PG contains multiple peaks like figure 1c, we must examine whether the most likely peak at P_0 can immediately be identified with P^*, or some other peaks must also be considered for their candidacy. Since $X(P)$ is no longer Gaussian-distributed, we must abandon the method used in subsection A2, to regard $X(P)$ as a variable obeying a chi-square distribution. Instead, we may invoke the Bayes's theorem, to derive

$$Q(P|X) = \frac{\alpha\, \mathcal{L}(X|P) \times Q(P)}{Q(X)}. \tag{8}$$

Here, $\alpha \geq 0$ is a constant, $Q(X)$ is the probability to observe the data $X \equiv X(P)$ of equation (7), $\mathcal{L}(X|P)$ is the likelihood of X against an assumed P, $Q(P)$ is the prior probability for P to represent the true period P^*, and $Q(P|X)$ is the posterior probability for the same statement after the data X are given.

By taking the ratio of equation (8) between P_0 and another period P, and substituting equation (7) into $\mathcal{L}(P)/\mathcal{L}(P_0) = \mathcal{L}(X|P)/\mathcal{L}(X|P_0)$, α and $Q(X)$ both cancel out to give

$$\frac{Q(P|X)}{Q(P_0|X)} = \frac{\mathcal{L}(X|P)Q(P)}{\mathcal{L}(X|P_0)Q(P_0)} = \exp\left\{-\frac{1}{2}X(P)\right\}\frac{Q(P)}{Q(P_0)}. \tag{9}$$

This gives a posterior probability, relative to P_0, for P to be the true period.

We applied equation (9) to the period fringes seen in the PG from G93T (figure 1c). The derived posterior probability of the n-th fringe, denoted as $Q_n \equiv Q(P_n|X)$, is given in table 3. Here, we set $Q(P)/Q(P_0) \equiv 1$, because we do not have any prior information as to the pulse period in 1993; the results from KE98, G93p or G3f should not be used because they are not independent from the G93T data, and the back extrapolation from the 1995 result is not constraining enough. See subsection 3.1 for the subsequent discussion.

A4: Evaluation of the T-fringes

The T-fringes seen in figure 6 have parameters as summarized in table 6. Their relative significance can be examined in the same way as in subsection A3, by replacing P in equation (9) with T and rewriting it as

$$\frac{Q(T_k|X)}{Q(T_0|X)} = \frac{\mathcal{L}(X|T_k)Q(T_k)}{\mathcal{L}(X|T_0)Q(T_0)} = \exp\left[-\frac{1}{2}X(T)\right]\frac{Q(T)}{Q(T_0)}. \tag{10}$$

Here, $T_0 = 16.435$ ks specifies the peak D, and T_k any other T-fringe peak. Assuming the true value of T to be the same between 1993 and 1995, we can utilize the G95 DeMD (black curve in figure 6) as the prior information, and write $Q(T)/Q(T_0) = \exp(-X_{95}/2)$, where X_{95} is the Z^2_4 decrement in the G95 DeMD from its peak value. The results of this calculation are summarized in the last three columns in table 6, and are utilized in subsubsection 3.3.2.

Appendix B: Significance of the DeMD peak

Using the 3–12 keV result from G95, we evaluate the significance of the DeMD peak at $T_{16.4}$. Instead of performing Monte-Carlo simulations, the actual G95 data themselves are used, after Makishima et al. (2021b). That is, we repeat the demodulaton computation in the same manner as in figure 2c, but scanning T from 0.05 ks to 6 ks, which is sufficiently longer than P but shorter than $T_{16.4}$. Because $T_{16.4}$ is close to three times

Table 6. Parameters of the peaks in the 2.55–12 keV DeMD from G93T.*

DeMD	T	$P^\dagger$	Z_4^2		Relative probability		
peak	(ks)	(s)	G93T	G95‡	G93T§	G95‖	total#
A	17.520 (42)	7.468 140	62.92	37.22	0.63	1.8×10^{-4}	1.2×10^{-4}
B	17.187 (58)	7.468 414	57.15	40.39	0.035	8.9×10^{-4}	3.2×10^{-5}
C	16.782 (39)	7.468 482	56.64	49.23	0.027	0.074	2.0×10^{-3}
C'	16.626 (16)	7.468 470	58.91	52.63	0.084	0.41	0.034
D	16.435 (24)	7.468 484	63.86	54.43	(1)	(1)	(1)
E	16.113 (35)	7.468 416	58.41	51.85	0.066	0.27	0.018
F	15.807 (30)	7.468 417	59.93	43.66	0.14	4.6×10^{-3}	6.5×10^{-4}
G	15.510 (27)	7.468 416	57.16	35.56	0.035	7.9×10^{-5}	2.8×10^{-6}

* Referring to the red DeMD in figure 6.
† Defined at the start of the G93pA data stream.
‡ The Z_4^2 value of the G95 DeMD in 3–12 keV.
§ Corresponding to the factor $\exp(-X/2)$ in equation (10).
‖ Corresponding to the relative prior probability $Q(T)/Q(T_0)$ in equation (10).
Representing the relative posterior probability $Q(T_k|X)/Q(T_0|X)$ of equation (10).

the orbital period of ASCA, $P_{\rm orb} \approx 5.5$ ks, the selected period range purposely covers $P_{\rm orb}$ and $2P_{\rm orb}$. To ensure Fourier independence between adjacent trials in T, its step is chosen as $\delta T \gtrsim T^2/S$, where $S \approx 112.4$ ks is the total data span. We treat A and ψ in the same manner as in the actual PPM analysis, and P is varied by ± 60 μs around the best period, 7.47384 s. The values of Z_m^2 thus obtained will represent its statistical plus systematic fluctuations under the actual observing condition.

The above *control* study yielded about 2100 *independent* trials in T, but in no cases Z_4^2 exceeded the target value, $Z_4^2 = 54.4$ (table 2); the highest was $Z_4^2 = 51.0$. Thus, the probability to obtain, by chance, a DeMD peak with $Z_4^2 \geq 54.4$ in a single trial in T becomes $\mathcal{P}_{\rm ch} < 1/2100 = 0.048\%$. The chance probability of the $T = 16.4$ ks peak is obtained by multiplying this $\mathcal{P}_{\rm ch}$ with the actual number of *independent* trials conducted in producing figure 2c over $T = 7 - 100$ ks. This is estimated as $S/7 - S/100 = 14.9$ in terms of the Fourier wave number. These finally yield $\mathcal{P}_{\rm ch} < 0.048\% \times 14.9 = 0.72\%$.

For further confirmation, we repeated the demodulation calculation at $T \approx P_{\rm orb} = 16.81 \pm 0.05$ ks (subsubsection 3.2.2) and $T \approx 2P_{\rm orb}$ with a finer step with $\Delta T = 0.01$ ks, but Z_4^2 remained ≤ 44.5. Since possible artifacts related to the ASCA's orbital period is thus signifiant at neither $T \approx P_{\rm orb}$ nor $T \approx 2P_{\rm orb}$, we reconfirm that the DeMD peak at $T = T_{16.4} \approx 3P_{\rm orb}$ is very unlikely to be instrumental.

From these evaluations, we can claim, at 99% or higher confidence, that the DeMD peak at $T_{16.4}$ in the 3–12 keV GIS95 data is real.

References

Appourchaux, T., L. Gizon, L., & Rabello-Soares, M.-C. 1998, A&A Suppl., 132, 107

Burke, B. E., et al. 1991, IEEE Trans., ED38, 1069

Butikov, E. 2006, Europ. J. Phys., 27, 1071

Enoto, T., et al. 2011, PASJ, 63, 387

Enoto, T., Nakazawa, K., Makishima, K., Rea, N., Hurley, K., & Shibata, S. 2010, ApJL, 722, L162

Ioka, K., & Sasaki, M. 2004, ApJ, 600, 296

Kouveliotou, C., et al. 1994, Nature, 368, 125

Kouveliotou, C., et al. 1998, Nature, 393, 235 (KEA98)

Landau, L. D., & Lifshitz, E. M. 1996, Mechanics (3rd.ed). Pergamon

Makishima, K. 2023, Proc. IAU, 363, 267

Makishima, K., et al. 1996, PASJ, 48,171

Makishima, K., Enoto, T., Hiraga, J. S., Nakano, T., Nakazawa, K., Sakurai, S., Sasano, M., & Murakami, H. 2014, Phys. Rev. Lett., 112, 171102

Makishima, K., Enoto, T., Murakami, H., Furuta, Y., Nakano, T., Sasano, M., & Nakazawa, K. 2016, PASJ, 68, S12

Makishima, K., Enoto, T., Yoneda, H., & Odaka, H. 2021a, MNRAS, 502, 2266

Makishima, K., Muakami, H., Enoto, T., & Nakazawa, K. 2019, PASJ, 71, 15

Makishima, K., Tamba, T., Aizawa, Y., Odaka, H., Yoneda, H., Enoto T., & Suzuki, M. 2021b, ApJ, 923, 63

Makishima, K., Uchida, N., Yoneda, H., Enoto T., & Takahashi, T. 2023, ApJ, 959, id.79

Mereghetti, S. 2008, A&AR, 15, 225

Murakami, T., Tanaka, Y., Kulkarni, S., Ogasaka, Y., Sonobe, T., Ogawara, Y., Aoki T., & Yosida A. 1994, Nature, 368, 127

Nakano, T., Murakami, H., Makishima, K., Hiraga, J. S., Uchiyama, H., Kaneda, H., & Enoto, T. 2015, PASJ, 67, id,9

Ohashi, T., et al. 1996, PASJ, 48, 157

Palmer, D. M., et al. 2005, Nature, 434, 1107.

Rea, N., Viganó, D., Israel, G. L., Pons, J. A., & Torres, D. F. 2014, ApJL, 781, L17.

Serlemitsos, P., et al. 1995, PASJ, 47, 105

Tanaka, Y., Inoue, H., & Holt, S. S. 1994, PASJ, 46, L37

Younes, G., Kouveliotou, C., & Kaspi, V. M. 2015, ApJ, 809, id. 165

Yoneda, H. 2020, PhD Thesis, The University of Tokyo, Appendix A